Low-Temperature Interquinone Electron Transfer in Photosynthetic Reaction Centers from *Rhodobacter sphaeroides* and *Blastochloris viridis*: Characterization of Q_B^- States by High-Frequency Electron Paramagnetic Resonance (EPR) and Electron−Nuclear Double Resonance (ENDOR)†

Lisa M. Utschig,* Marion C. Thurnauer, David M. Tiede, and Oleg G. Poluektov

Chemistry Division, Argonne National Laboratory, Argonne, Illinois 60439

Received June 3, 2005; Revised Manuscript Received September 6, 2005

ABSTRACT: High-frequency electron paramagnetic resonance (HF EPR) techniques have been employed to look for localized light-induced conformational changes in the protein environments around the reduced secondary quinone acceptor (Q_B^-) in *Rhodobacter sphaeroides* and *Blastochloris viridis* RCs. The Q_A^- and Q_B^- radical species in Fe-removed/Zn-replaced protonated RCs substituted with deuterated quinones are distinguishable with pulsed D-band (130 GHz) EPR and provide native probes of both the low-temperature $Q_A^-Q_B \rightarrow Q_AQ_B^-$ electron-transfer event and the structure of trapped conformational substates. We report here the first spectroscopic evidence that cryogenically trapped, light-induced changes enable low-temperature $Q_A^-Q_B \rightarrow Q_AQ_B^-$ electron transfer in the *B. viridis* RC and the first observation of an inactive, trapped $P^+Q_B^-$ state in both *R. sphaeroides* and *B. viridis* RCs that does not recombine at 20 K. The high resolution and orientational selectivity of HF electron−nuclear double resonance (ENDOR) allows us to directly probe protein environments around Q_B^- for distinct $P^+Q_B^-$ kinetic RC states by spectrally selecting specific nuclei in isotopically labeled samples. No structural differences in the protein structure near Q_B^- or reorientation (within 5°) of Q_B^- was observed with HF ENDOR spectra of two states of $P^+Q_B^-$: "active" and "inactive" states with regards to low-temperature electron transfer. These results reveal a remarkably enforced local protein environment for Q_B in its reduced semiquinone state and suggest that the conformational change that controls reactivity resides beyond the Q_B local environment.

Electron-transfer reactions within membrane proteins occur between specifically positioned donor and acceptor cofactor molecules intricately anchored in a polypeptide environment. The interactions of the protein matrix with the cofactors are essential both for fine-tuning electron-transfer reactions and for coupling these reactions with secondary reactions, such as proton transfer. However, the experimental determination of the local protein−cofactor interactions that affect these processes remains a challenge. The photosynthetic bacterial reaction center (RC)[1] is an important model system for gaining insight into these factors. The RC is an integral membrane protein that couples light-induced, sequential electron transfer with proton-transfer reactions. High-resolution crystal structures show that the bacterial RC from *Rhodobacter sphaeroides* (*1*−*3*) consists of three 30−35 kDa protein subunits, L, H, and M, which bind nine cofactors: four bacteriochlorophylls (Bchl), two bacteriopheophytins (Bph), two ubiquinones (Q), and one internally bound nonheme iron. In the RC, electron transfer occurs sequentially following photoexcitation of a bacteriochlorophyll dimer (P), through one set of cofactors, to a quinone molecule Q_A within 150−250 ps, resulting in a metastable charge-separated state, $P^+Q_A^-$ (*4*, *5*). Subsequently, within about 200 μs, the electron reaches the final quinone acceptor Q_B, which functions as a two-electron, two-proton acceptor following two successive turnovers of the RC photochemistry (*6*).

The heterogeneous kinetics, temperature trends, and pH dependencies of the $Q_A^-Q_B \rightarrow Q_AQ_B^-$ reaction show that this interquinone electron transfer in isolated RCs is intimately linked to a complex conformational landscape (*7*−*13*). The rate of the $Q_A^-Q_B \rightarrow Q_AQ_B^-$ electron transfer at room temperature is independent of the driving force for the reaction, at least for the main ∼100 μs component (*9*) seen in isolated *R. sphaeroides* RCs, demonstrating that this step is limited by a protein conformational change (*14*). Low-temperature kinetics also indicate that a structural change accompanies the first interquinone electron-transfer step. $Q_A^-Q_B \rightarrow Q_AQ_B^-$ electron transfer is not observed at low temperatures (<200 K) for RCs frozen in the dark. However, electron transfer between the quinones does occur at cryogenic temperatures for *R. sphaeroides* RCs frozen under illumination (so-called "Kleinfeld effect") (*15*). These observed alterations of reaction kinetics have been linked to

† This work was supported by the U.S. Department of Energy, Office of Basic Energy Sciences, Division of Chemical Sciences, Geosciences, and Biosciences, under contract W-31−109-Eng-38.

* Corresponding author. Phone, (630) 252-3544; fax, (630) 252-9289; e-mail, utschig@anl.gov.

[1] Abbreviations: RC, reaction center; EPR, electron paramagnetic resonance; ENDOR, electron−nuclear double resonance; P, primary electron donor; Q_A and Q_B, primary and secondary quinone electron acceptors; FTIR, Fourier transform infrared spectroscopy; HF, high-frequency; EDTA, ethylenediaminetetraacetic acid; LDAO, lauryldimethylamine *N*-oxide; DAF, delay after laser flash; ESE, electron spin echo; ^{1}H, proton; ^{2}H, deuteron.

10.1021/bi051060q CCC: $30.25
Published on Web 10/08/2005

trapping the RC in altered conformations induced by charge separation (*15*).

The nature of these light-induced structural changes in RCs having both quinones bound remains a mystery. Similarly, RCs that lack Q_B exhibit a light-induced structural change. This is evidenced by the remarkably prolonged lifetime of the radical pair state $P^+Q_A^-$ formed from RCs cooled to cryogenic temperatures under illumination compared with RCs frozen in the dark (*15*). Transient electron paramagnetic resonance (EPR) spectra of the electron spin-polarized $P^+Q_A^-$ state from RCs frozen in the light and the dark were examined, and it was determined that the altered recombination kinetics for the former case were not the result of reorientation of the cofactors P^+ and Q_A^- (*16*, *17*). Herein, the light-induced structural changes that are necessary for $Q_A^-Q_B \rightarrow Q_AQ_B^-$ electron transfer to occur at low temperature are examined, with a focus on the local protein structure surrounding Q_B^-.

The low-temperature reaction kinetics have been proposed to be linked to two distinct sites of Q_B, the "distal" and "proximal" positions, observed in *R. sphaeroides* RC crystal structures. The position of Q_B^- as determined from X-ray crystal structures of light-adapted RC crystals in the charge-separated state $P^+Q_B^-$ is located approximately 5 Å from the Q_B position in the charge-neutral state, PQ_B, and has undergone a 180° propeller twist around the isoprene chain (*18*). This significant shift in position and rotation of Q_B in the light-adapted structures relative to those adapted in the dark led to the proposal that the proximal and distal Q_B positions correspond to active and inactive conformations with respect to electron transfer from Q_A^- to Q_B and that movement between these two configurations represents the conformational gate for this reaction (*18*). Thus, for RCs frozen in the dark, it was suggested that Q_B is locked in the distal or "inactive" conformation, whereas Q_B is shifted to the proximal or "active" conformation for RCs frozen in the light. Recent experimental results contradict this proposal, and the correlation between the shift in Q_B configuration and rate-limiting conformational change has not been fully established (*13*, *19*−*22*). In fact, Fourier transform infrared (FTIR) spectroscopic data, as well as optical measurements of structurally characterized RC mutants with Q_B in the proximal position, argue against a large-scale, light-induced shift in the position of Q_B as a part of the gating mechanism for RCs in noncrystalline states (*13*, *23*−*25*).

A conformational intermediate between the dark state and light-induced state was detected with transient optical measurements of RCs which were frozen under illumination and then allowed to relax partially at 120 K from a light-adapted to a dark-adapted conformation (*12*). In general, optical experiments are often complicated because there is no primary optical marker to distinguish between the semiquinone states Q_A^- and Q_B^- (both ubiquinone-10 in *R. sphaeroides* RCs) (*9*). Thus, secondary electrochromic markers that monitor the charge distribution are often used in optical experiments (*8*, *26*, *27*). However, with this approach, it is difficult to distinguish between electron transfer and secondary processes, such as proton transfer or protein rearrangement (*8*, *28*). Magnetic resonance techniques have the potential to allow direct investigation of conformational intermediates by examining the semiquinone cofactor structures and local protein conformations surrounding the quinones, as well as the radical pairs $P^+Q_A^-$ and $P^+Q_B^-$ (*29*). For example, at high-frequency Q_A^- and Q_B^- have resolved *g*-tensors, and thus, EPR signals of Q_A^- and Q_B^- can be distinguished from each other. This resolution allows the quinone electron-transfer processes to be directly monitored, albeit at low temperatures.

In contrast to data from X-ray crystallography, EPR spectroscopy can provide structural information concurrent with functional data for RCs in solution. Crystallization conditions and the inherent labile nature of Q_B cause concerns about the occupancy of the Q_B site and the ability of Q_B to accept an electron in the crystals (*22*, *30*). The possibility of radiation damage to the protein complicates interpretation of X-ray data (*31*, *32*). Although many studies of crystal structures for both *Blastochloris viridis* and *R. sphaeroides* RCs have focused on the problem of the location of Q_B (*3*, *18*, *19*, *21*, *22*, *30*, *33*, *34*), no consensus about the functional relevance of the multiple structurally determined quinone binding sites has been achieved. One important advantage of EPR spectroscopy is that localized structural information can be obtained for a known redox state of the Q_B, that is, the semiquinone Q_B^- radical state. In general, there are only a few magnetic resonance studies of Q_B^- due to difficulties of generating this radical species in the *R. sphaeroides* RC (*29*). No EPR studies of Q_B^- in *B. viridis* RC have been reported.

We have initiated new methodologies that utilize both specialized samples and high-frequency (HF) pulsed EPR techniques and have applied these methods to investigate light-induced protein conformational substates related to low-temperature $Q_A^-Q_B \rightarrow Q_AQ_B^-$ electron transfer. Protonated Fe-removed/Zn-replaced bacterial reaction center samples substituted with fully deuterated quinones were prepared for these studies. HF D-band (130 GHz/4.6 T) EPR spectra of these samples display resolved P^+, Q_A^-, and Q_B^- radical signals. The structures of distinct Q_B^- substates and the associated electron-transfer reaction kinetics at low temperature for RCs trapped in different conformational substates were spectroscopically examined. Furthermore, HF Mims-type pulsed electron−nuclear double resonance spectroscopy (ENDOR), or "matrix" ENDOR, has been applied to directly look for differences in the protein environments surrounding the quinones. Selective deuteration of the quinone, in a protonated protein environment, allows for spectral features of the quinone radicals to be distinguished in the ENDOR experiment from protein environments or "matrix" surrounding the quinone radicals. In this report, we have used these techniques to examine structural changes to the immediate Q_B^- environment for *R. sphaeroides* RCs frozen under illumination in active or inactive states of $P^+Q_B^-$. We have extended these studies to the RC from *B. viridis* where we have observed the so-called "Kleinfeld effect" (*15*). Thus, light-induced changes that enable low-temperature $Q_A^-Q_B \rightarrow Q_AQ_B^-$ electron transfer in *B. viridis* RCs can be trapped cryogenically and are not dependent on the non-heme Fe^{2+}.

EXPERIMENTAL PROCEDURES

Preparation of Fe-Removed/Zn-Substituted Protonated RCs Substituted with Deuterated Quinone. The non-heme Fe^{2+} is magnetically coupled to the quinones, giving rise to a broad $[Fe^{2+}Q_A]^-$ resonance centered at $g \sim 1.8$ (*35*, *36*).

In the absence of the paramagnetic metal, the quinone signal narrows to that of a typical organic radical with $g = 2.0049$. Thus, for both *R. sphaeroides* and *B. viridis* RCs, the Fe^{2+} needs to be removed and replaced with diamagnetic Zn^{2+} in order to observe resolved *g*-tensors in the EPR experiment. Zn^{2+} was substituted into the Fe site using a modification to the procedure of Utschig (*37*), as recently reported (*38*).

Purified protonated RCs from *R. sphaeroides* R-26 (1.0 mL $OD_{803} \sim 25$ cm^{-1} in 10 mM Tris-HCl, pH 7.8, 10 μM EDTA, 280 mM NaCl, and 0.045% LDAO) were incubated with 2.4 mM *o*-phenanthroline and 1.0 M LiSCN for 30 min on ice. Then, 1 mM $ZnSO_4$ and 9 mM 2-mercaptoethanol were added, and the protein was again incubated on ice for 30 min, followed by dialysis at 4 °C against 10 mM HEPES, pH 7.9, 20 mM NaCl, 0.045% LDAO, and 6 g of Chelex 100 metal-chelating resin (BioRad) for 48 h, with several changes of buffer. Following dialysis, precipitated materials were removed by centrifugation. The Fe-removed/Zn-replaced RCs were incubated with 4 equiv of deuterated ubiquinone-10 obtained from whole cells of *R. sphaeroides* R-26 grown in D_2O (99.7%) on deuterated substrates. Samples were concentrated with centricon-50 or microcon-50 ultrafiltration devices (Amicon); 20% glycerol was added. Samples were frozen with liquid nitrogen and stored at −80 °C. Comparison of experimentally determined ratios of the light-induced $P^+Q_A^-$ charge-separated state to simulated P^+ and Q_A^- signals expected for total paramagnetic metal ion depletion indicates that >90% of the Fe^{2+} has been removed.

Fe-removal/Zn-replacement in purified *B. viridis* RCs was accomplished by a similar procedure as described above for *R. sphaeroides* RCs. Purified protonated RCs from *B. viridis* (1.0 mL $OD_{830} \sim 17$ cm^{-1} in 10 mM Tris-HCl, pH 7.8, 10 μM EDTA, 150 mM NaCl, and 0.045% LDAO) were incubated on ice in 2.4 mM *o*-phenanthroline, 9 mM Tris-HCl, 140 μM menatetrenone (Sigma), and 0.8 M LiSCN. After 20 min, 1 mM $ZnSO_4$ and 9 mM 2-mercaptoethanol were added, and the protein was again incubated on ice. After 20 min, the protein was transferred to 10-mm-wide 12-14000 MWCO dialysis tubing (Spectra/Por) and dialyzed 48 h at 4 °C against 10 mM HEPES, pH 7.9, 20 mM NaCl, 0.045% LDAO, and 6 g of Chelex 100 metal-chelating resin (BioRad), with several changes of buffer. Following dialysis, precipitated materials were removed by centrifugation. The protein was incubated with 4 equiv of deuterated ubiquinone-10. The samples were concentrated and frozen as detailed above for *R. sphaeroides* RCs. At X-band, the light-induced Boltzmann signals from P_{960}^+ and Q_A^- overlap, resulting in a derivative signal at $g = 2.0037$ that is asymmetric (less intense and broader at high field than low field), indicating removal of the paramagnetic Fe^{2+} (*37*). At high-field, the P_{960}^+ and Q_A^- signals are resolved; however, exact estimates of the amount of Fe-removal at high-field based on the ratios of light-induced steady-state P_{960}^+ to Q_A^- signals are complicated by the presence of the bound cytochrome, which reduces the intensity of P_{960}^+. Comparison of the observed signal intensities of Q_A^- and Q_B^- for *B. viridis* to signals observed for analogous samples of *R. sphaeroides* indicates that >50% of the Fe^{2+} has been removed from the *B. viridis* RC.

Q_B replacement with the inhibitor stigmatellin was accomplished by the addition of 10−15 mol equiv of stigmatellin (Fluka, 20 mM stock solution in 10% ethanol) per RC molecule to diluted Fe-removed/Zn-substituted RCs (~60 μM RC). Precipitate was spun down, and samples were concentrated to 300−500 μM RC with microcon-50 ultrafiltration devices. For samples with chemically reduced Q_A^-, 20% glycerol and 6 mM sodium hydrosulfite (Sigma, 126 mM stock in 1 M Tris-Cl, pH 8.0) were added under a nitrogen atmosphere, followed by shock-freezing in liquid nitrogen.

D-Band EPR and ENDOR Spectroscopy. HF EPR and ENDOR measurements were performed on a pulsed/continuous wave HF D-band (130 GHz/4.6 T) EPR spectrometer, as described previously (*38*, *39*). Pulsed EPR spectra were recorded by monitoring the electron spin echo (ESE) intensity from a two-microwave pulse sequence as a function of magnetic field. Time-resolved EPR spectra were recorded using a two-pulse sequence, which followed a 5 ns laser pulse at a fixed delay after laser flash (DAF) time. Pulsed ENDOR spectra were recorded using a Mims- (*40*) or Davis-type (*41*) sequence of microwave and radio frequency (RF) pulses by monitoring the ESE intensity as a function of the frequency of the RF pulse. A fast-pulse programming/acquisition system developed on the basis of a 1 GHz arbitrary waveform generator PC card AWG1000 (Chase Scientific Co.) by Dr. A. Astaskin, University of Arizona, was employed. RF pulses were generated by an Agilent RF signal generator (model E4400B) and amplified by a 1 kW pulsed amplifier (CPC, model 5T1000). For the ^1H ENDOR experiment, the duration of the π_{RF}-pulse was around 20 μs, while for the ^2H-ENDOR, the duration of the π_{RF}-pulse was around 50 μs. All EPR and ENDOR spectra were recorded at 20 K with 10 Hz repetition rate using the same pulse sequences. For the EPR spectra, $\pi/2$ microwave pulse was 60 ns, τ-time was 200 ns. For Mims-type ^1H ENDOR spectra, $\pi/2$ microwave pulse was 60 ns, τ-time was 200 ns, *T*-time was 25 μs.

Samples were placed in quartz tubes (i.d. 0.5 mm/o.d. 0.6 mm) within the single mode cylindrical TE_{011} cavity, having slits to allow for optical and RF excitation. The temperature was controlled by an Oxford temperature control system. Kinetic measurements at low temperatures were performed either by following the time-evolution of the ESE signal after a single laser flash, so-called DAF-experiment, or by monitoring the ESE intensity after on/off switching of the laser during a series of laser pulses at 10 Hz.

Illumination Conditions. The RC samples were frozen in the light by two separate methods. For the first method of trapping Q_B^- (termed the "laser regime"), the samples were placed in the cavity and then frozen under continuous laser flashing. These samples were cooled from room temperature to 20 K with 1 Hz laser excitation at 605 nm, 0.5 mJ/pulse with optical parametric oscillator (Opotek) pumped by a Nd:YAG laser (Quantel). The output of the laser was coupled to a fiber optic to deliver light to the sample in the cavity (~0.2 mJ/pulse). The second method (termed the "red light regime") involved illuminating RC samples for 3 s with a Xenon lamp having a red band-pass filter (600−650 nm) followed by shock-freezing of the sample in liquid N_2. These samples were rapidly transferred, in the dark, from the liquid N_2 into the cavity pre-cooled at 20 K. The cavity warmed to ~70−100 K during the sample insertion procedure.

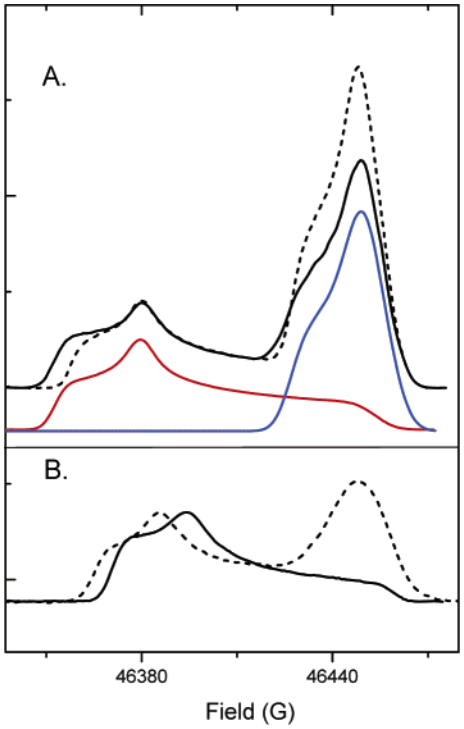

FIGURE 1: D-band (130 GHz) two-pulse, echo-induced field swept (ESE) EPR spectra recorded at 20 K. (A) Protonated Fe-removed/Zn-replaced *R. sphaeroides* RCs substituted with deuterated UQ-10: $P^+Q_A^-$ signal (solid line) was recorded by laser pulse excitation for a sample frozen in the dark. $P^+Q_B^-$ signals (dotted line) were generated by cooling RCs from room temperature to 20 K under 1 Hz, 605 nm laser excitation. Simulated spectra of P^+ (blue line) and Q_A^- (red line) are shown for comparison. (B) Protonated Fe-removed/Zn-replaced *B. viridis* RCs substituted with deuterated UQ-10: Q_A^- signal (solid line) was observed for chemically reduced protonated menaquinone in *B. viridis* RCs. $P^+Q_B^-$ signal (dotted line) was observed for samples cooled from room temperature to 20 K under 1 Hz, 605 nm laser excitation.

RESULTS

HF EPR Spectra of $P^+Q_A^-$ and $P^+Q_B^-$ from R. sphaeroides and B. viridis RCs. D-band (130 GHz) two-pulse, electron spin−echo (ESE) induced field swept EPR spectra of protonated Fe-removed/Zn-replaced *R. sphaeroides* RCs substituted with deuterated UQ-10 are shown in Figure 1A. ESE signals of the transient $P^+Q_A^-$ state generated at 20 K by laser pulse excitation were obtained for samples frozen in the dark. $P^+Q_B^-$ states were generated by cooling the sample from room temperature to 20 K under 1 Hz, 605 nm laser excitation. Identical $P^+Q_B^-$ spectra were obtained for RCs shock-frozen in liquid nitrogen after a 3 s exposure to red light at room temperature. A slight broadening of lines in the spin-correlated electron pair spectrum for the protonated RCs substituted with deuterated Q_A with respect to observed spectral lines for fully deuterated RCs (*37*) suggests that at most 20% of Q_A is protonated. A higher percent of incorporation of deuterated Q_B (>90%) compared to Q_A is expected due to the easier reconstitution of Q_B following the inherent loss of native Q_B during RC purification (*8*) and the initial Fe-removal/Zn-replacement procedures (*37*). The *g*-tensors of Q_A^- and Q_B^- measured at HF EPR are listed in Table 1. The deviation of these *g*-values from those previously obtained (*29*) is due mainly to different *g*-value calibration procedures, as previously described (*42*). Importantly, the high resolution of the *g*-tensors at HF EPR allows us to distinguish the resonances of Q_A^- and Q_B^- and, thus, especially at low field resonances, allows the direct examination of the formation or decay of each quinone species at low temperature.

Table 1: Semiquinone Anion Radical *g*-Tensor Principle Values Obtained from the Experimental D-Band (130 GHz) EPR Spectra of Fe-Removed RCs from *R. sphaeroides* and *B. viridis*[a]

	R. sphaeroides		*B. viridis*	
	Q_A^-	Q_B^-	Q_A^-	Q_B^-
g_x	2.00667	2.00644	2.00618	2.00640
g_y	2.00552	2.00551	2.00511	2.00550
g_z	2.00233	2.00232	2.00234	2.00233
g_{av}	2.00484	2.00476	2.00454	2.00474

[a] Mn^{2+} in MgO was used as a reference sample for the measurement of *g*-tensor values. Calibration procedure is described in detail in refs *42*, *47*. In the case when g_z part of the quinone anion spectrum overlaps with donor cation spectrum, g_z was reconstructed by subtracting two spectra having different relative intensities of Q^- and P^+. Absolute values of the *g*-tensors were measured with an accuracy of 1×10^{-4}. The relative values of the *g*-tensors within one radical species were determined with an accuracy of 5×10^{-5}.

Unlike the *R. sphaeroides* RC, the RC from *B. viridis* contains two different quinones in the Q_A and Q_B sites and also has a tightly bound cytochrome subunit containing four heme molecules (*43*). The primary quinone, Q_A, is a menaquinone, and the secondary quinone, Q_B, is a ubiquinone-9. By similar methods applied to *R. sphaeroides* RCs described above, we were able to trap and distinguish the EPR signal of protonated menaquinone Q_A^- from the signal of deuterated ubiquinone-10 Q_B^- in *B. viridis* RCs (Figure 1B). To our knowledge, this is the first report of the Q_B^- EPR signal in *B. viridis* RCs. As expected, the *g*-values for Q_A^- menaquinone in *B. viridis* (*44*) are shifted from those of the Q_A^- ubiquinone in *R. sphaeroides* (*29*), and these differences are resolved at high-frequency EPR. The *g*-values of Q_B^- in *B. viridis* and *R. sphaeroides* are nearly identical (Table 1) indicating similar electronic structures and H-bonding for Q_B^- in the different species (*45*).

Trapping Kinetically Distinct Substates at Low Temperature. EPR spectroscopy reveals two kinetically distinct conformational substates of $P^+Q_B^-$ for *R. sphaeroides* RCs frozen in the light: an "**inactive**" $P^+Q_B^-$ state and an "**active**" $P^+Q_B^-$ state. A typical sample frozen under illumination contained both a fraction of the "inactive" state and a fraction of the "active" state, as determined by direct monitoring of the EPR signals of $P^+Q_B^-$. For the inactive state, $P^+Q_B^-$ is trapped with no charge recombination occurring at 20 K and is detected as a static $P^+Q_B^-$ EPR signal. We believe that this is the first report of an inactive $P^+Q_B^-$ state. The active $P^+Q_B^-$ state is observed by an increase in intensity of the $P^+Q_B^-$ EPR signal at 20 K upon continuous 10 Hz laser excitation at 605 nm and a decay of this fractional signal increase of the $P^+Q_B^-$ EPR signal after the light is turned off.

An example of EPR signals representing inactive $P^+Q_B^-$ and active $P^+Q_B^-$ states observed after RCs were frozen with the red light regime is shown in Figure 2. A static $P^+Q_B^-$ signal reflecting the inactive state is observed at 20 K, in the dark. The population of RCs that are active to low-temperature $Q_A^-Q_B \rightarrow Q_AQ_B^-$ electron transfer is observed by the increased intensity of the $P^+Q_B^-$ signal when the sample is continuously flashed with a 10 Hz laser light at

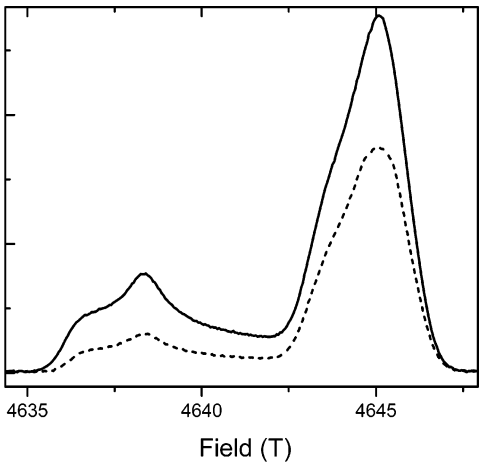

FIGURE 2: D-band ESE EPR spectra obtained for *R. sphaeroides* RCs frozen in liquid nitrogen after a 3 s exposure to red light at room temperature. $P^+Q_B^-$ spectra were acquired at 20 K in the dark (dotted line) and under 10 Hz continuous flashing conditions, 605 nm laser excitation (solid line).

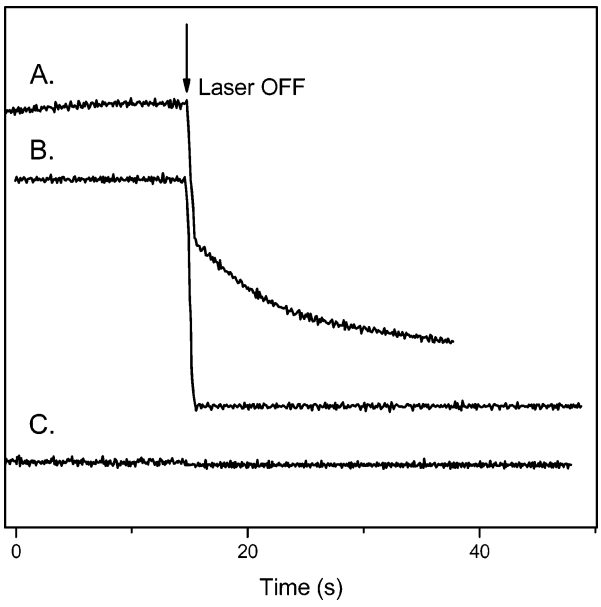

FIGURE 3: Kinetics measured at 20 K by monitoring the decay of the EPR signal at 46382 G after turning the laser off. Typically, samples frozen under illumination exhibited a combination of kinetics for "inactive" and "active" states. The traces shown here were obtained from samples having primarily one state present. (A) Slow, distributed multiexponential decay on the order of 10 s, 30 s, and 2 min was observed for Q_B^- in the "active" state. The sample was frozen with the red light regime. (B) A single decay of ~70 ms is observed for samples where electron transfer to Q_B is blocked by stigmatellin, consistent with recombination from Q_A^-. This sample was frozen with the laser regime. (C) The Q_B^- signal does not decay for samples where Q_B^- is trapped in the "inactive" state. All (100%) of the inactive $P^+Q_B^-$ state was generated by irradiation of the RC with 5 Hz, 605 nm laser excitation during the cooling process.

20 K. Trace A, Figure 3 shows the decay in the signal at field position 46382 G, (corresponding to the g_y canonical component of Q_B^-) that occurs once laser excitation stops. The small rise in signal before laser excitation stops is due to $Q_A^-Q_B \rightarrow Q_AQ_B^-$ electron transfer, and the fast decay component is due to decay of Q_A^-. A slow distributed multiexponential decay component was observed for the active Q_B^-, from which decay constants of ~10 s, ~30 s, and ~2 min can be obtained. These kinetics differ from the faster signal decay kinetics of ~70 ms measured for Q_A^- that is observed for RCs frozen in the "dark" state or frozen under illumination in the presence of competitive inhibitors of Q_B (Trace B, Figure 3). A ~70 ms decay is consistent with charge recombination of $P^+Q_A^-$, indicating that no forward electron transfer occurs past Q_A^- at low temperature.

Different ratios of inactive state to active state were observed when the samples were trapped with the two light regimes: cooling the sample to 20 K under 1 Hz, 605 nm laser excitation (laser light regime) versus freezing the sample after a 3 s exposure to red light at room temperature (red light regime). For instance, a larger amount of active $P^+Q_B^-$ state versus inactive $P^+Q_B^-$ state was observed for samples frozen with the red light regime, whereas a larger amount of inactive $P^+Q_B^-$ state versus active $P^+Q_B^-$ state was created for samples frozen with the laser light regime. In fact, 100% of the inactive Q_B^- state can be generated when more intense light conditions are used, such as irradiation with 5 Hz laser flashes during the cooling process. This completely inactive $P^+Q_B^-$ state, as monitored by the Q_B^- signal at field position 46382 G, remained unchanged with and without laser excitation (Trace C, Figure 3). It is important to note that the observed differences in generating the inactive and active states with respect to light regime used could be the result of a combination of factors, including red versus orange light, continuous wave light versus pulsed light, as well as the actual procedures for freeze-trapping, that is, room-temperature irradiation followed by shock-freeze versus pulsed light irradiation of the samples while freezing.

The inactive $P^+Q_B^-$ signal can be quenched when the temperature is raised. For example, ~30% recombination of Q_B^- with P^+ occurs after warming the sample to 70 K for 60 min. Interestingly, when samples frozen to 20 K under laser light excitation were warmed to 170 K for 60 min, complete recombination of the inactive $P^+Q_B^-$ was observed (i.e., no $P^+Q_B^-$ signal remained after cooling this sample back to 20 K). However, ~50% of the RCs were still able to transfer electrons between Q_A^- and Q_B (active state), as observed by the increase in the $P^+Q_B^-$ signal generated in this sample by continuous 10 Hz flashing at 20 K. The Q_B^- signal for this sample exhibited a slow biexponential decay at 20 K with decay constants of 3 and 40 s. These kinetics differ from the multiexponential kinetics (~10 s, ~30 s, and ~2 min) observed for the active state at 20 K prior to warming the sample to higher temperatures.

$Q_A^-Q_B \rightarrow Q_AQ_B^-$ electron transfer can be monitored by watching spectral changes observed with DAF flash experiments (Figure 4). The dotted and dashed spectra reflect a mixture of signals from Q_A^- and Q_B^- due to the electron transfer at low temperature and can be compared to the steady-state EPR signals of Q_A^- and Q_B^- (solid lines). The decay time of the Q_B^- signal is too long to easily measure the direct formation of Q_B^-. However, the observed reaction states from the DAF experiments are used for determining the relative amounts of Q_A^- and Q_B^- present under continuous flashing conditions of the RC for the ENDOR experiments described below (Figure 9).

Low-Temperature $Q_A^-Q_B \rightarrow Q_AQ_B^-$ Electron Transfer in B. viridis RCs: The "Kleinfeld Effect". Similar to *R. spheroides* RCs, illumination of dark-adapted *B. viridis* RCs at 20 K yields signals only from $P^+Q_A^-$. Thus, low-

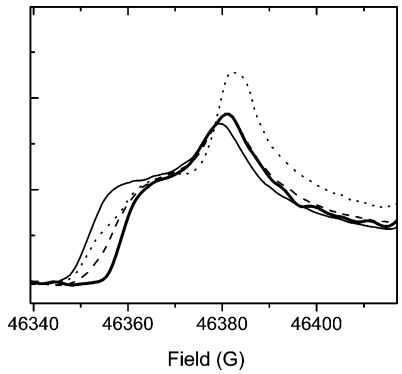

FIGURE 4: Spectral changes and measured electron-transfer kinetics indicate that an electron is transferred from Q_A^- to Q_B at 20 K for *R. sphaeroides* RCs frozen in the light. Spectra measured with 3 μs (dotted line) and 5 ms (dashed line) DAF experiments are compared to Q_B^- (bold line) and Q_A^- signals (solid line) generated as described in Figure 1A. The magnetic field range displayed shows only the g_x and g_y *g*-tensor components.

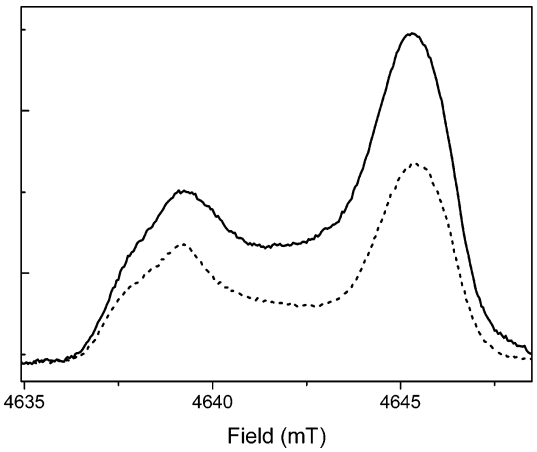

FIGURE 5: D-band ESE EPR spectra obtained for *B. viridis* RCs frozen in liquid nitrogen after a 3 s exposure to red light at room temperature, cooled to 20 K, then warmed to 170 K for 70 min in the cavity. $P^+Q_B^-$ spectra were acquired at 20 K in the dark (dotted line) and under 10 Hz continuous flashing conditions, 605 nm laser excitation (solid line).

temperature $Q_A^-Q_B \rightarrow Q_AQ_B^-$ electron transfer does not proceed in the dark-adapted state of the *B. viridis* RC. *B. viridis* RCs frozen in the light were examined to see if an electron could be transferred from Q_A^- to Q_B at low temperature. Samples frozen by cooling with the laser light regime had a large inactive $P^+Q_B^-$ signal at 20 K. The ratio of the P^+ EPR signal to the Q_B^- signal suggests that the tightly bound cytochrome in *B. viridis* possibly donated an electron to P^+ during cooling. The amplitude of the $P^+Q_B^-$ signal did not increase with 10 Hz laser excitation at 20 K, indicating that none of the RCs could transfer electrons to Q_B^- when frozen under the laser light regime. After annealing at 200 K for 30 min, the inactive $P^+Q_B^-$ signal at 20 K decreased to ~20% of its amplitude before annealing. A 10 Hz light excitation of this quenched sample showed that the electron is transferred only to Q_A, as a spin correlated radical pair (SCRP) spectrum consistent with $P^+Q_A^-$ is observed. Hence, no low-temperature $Q_A^-Q_B \rightarrow Q_AQ_B^-$ occurred under these conditions.

A second sample was frozen with the red light regime, the procedure that generated the largest component of active $P^+Q_B^-$ in *R. sphaeroides* RCs. A large inactive $P^+Q_B^-$ signal was observed. However, an additional signal from an active $P^+Q_B^-$ state was detected as a light-induced increase in the $P^+Q_B^-$ signal upon continuous 10 Hz laser flashing at low temperature. This active $P^+Q_B^-$ signal indicates low-temperature $Q_A^-Q_B \rightarrow Q_AQ_B^-$ electron transfer (Figure 5). Unlike *R. sphaeroides* RCs, low-temperature charge recombination did not occur for this active fraction. This sample was warmed to 170 K for 70 min to allow some conformational relaxation of the protein. About 50% of the $P^+Q_B^-$ signal was quenched, and once the protein was cooled back down to 20 K, $Q_A^-Q_B \rightarrow Q_AQ_B^-$ electron transfer was observed for a fraction of the RCs by an increase in the $P^+Q_B^-$ signal. Oxidation of the cytochrome subunit, before "light treatment", would be expected to increase the amounts of active Q_B^- at low temperature; however, this experiment remains a challenge because of difficulties with sample preparation. Nevertheless, the observation that an active fraction of RCs exhibits low-temperature electron transfer is the first experimental evidence that low-temperature interquinone electron transfer is possible in *B. viridis* RCs. Freezing RCs in the light induces a structural change that allows low-temperature $Q_A^-Q_B \rightarrow Q_AQ_B^-$ electron transfer to proceed in *B. viridis* RCs, similar to the "Kleinfeld effect" that was observed in *R. sphaeroides* RCs (*15*).

Probing Protein Environments with HF Mims-type ENDOR. The enhanced spectral resolution obtained with HF EPR allows complete resolution of the *g*-tensor components of the radical species in bacterial RCs (see above) (*42*, *46*−*48*). This enhanced resolution also permits the detection of small changes in magnetic resonance parameters that contain information on weak interactions between radicals and the protein environment. At D-band microwave frequency, the EPR signal of Q_B^- is well-resolved from the P^+ resonances, and HF ^{1}H ENDOR spectra can be obtained at magnetic field positions within the Q_B^- domain. Mims-type ^{1}H ENDOR is very sensitive to nuclei with small hyperfine interactions (HFI), allowing for observation of HFI with distant nuclei, that is, from the protein environment, the so-called matrix ENDOR (*38*, *40*, *49*, *50*). In the fully protonated RCs substituted with deuterated quinone, ^{1}H ENDOR performed on the Q_B^- EPR line is a pure matrix ENDOR with respect to this radical, because, first, Q_B^- does not contain any protons and, second, the frequency domains of ^{1}H and ^{2}H ENDOR spectra are well-separated at HF EPR. Thus, all nuclei which contribute to the ^{1}H ENDOR spectrum are from the protein environment and bound water molecules.

Orientational Selectivity. To apply these methods to examine changes in quinone environments, we "calibrate" and measure the sensitivity to small changes in radical orientation. The Mims-type ^{1}H ENDOR spectra were recorded at two different field positions, 3 G apart, within the photoaccumulated Q_B^- resonance domain. A 3 G magnetic field shift corresponds to an effective rotation of the radical by ~5° (Figure 6). Discernible differences in the HF ENDOR spectrum are detected with a mere 5° effective rotation of the *g*-tensor axis, demonstrating the sensitivity of HF Mims-type ENDOR to reorientation of the quinone.

Sensitivity to Local Structure. Since a large number of overlapping resonances from the protein contribute to the HF Mims-type, or "matrix", ENDOR spectra, direct assignment of the resonances is not possible. Hence, we look for differences between spectra from samples generated under

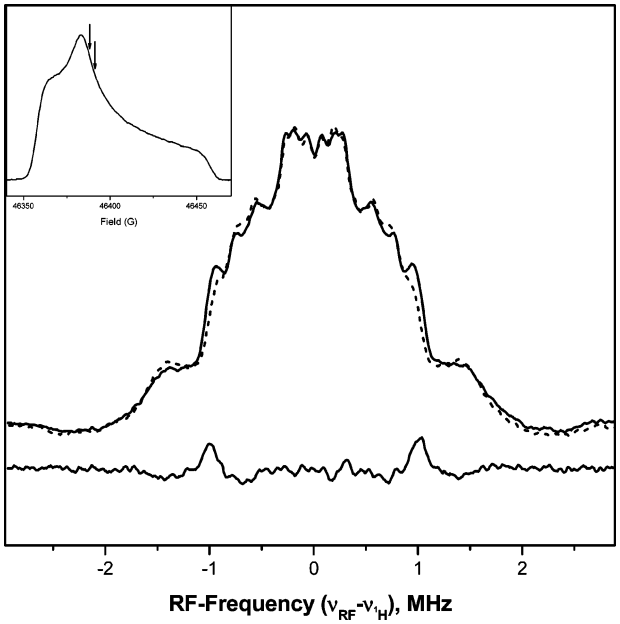

FIGURE 6: Orientational selectivity of D-band Mims-type ^{1}H ENDOR of Fe-removed/Zn-replaced RCs substituted with deuterated UQ-10 for *R. sphaeroides* RCs. ^{1}H ENDOR spectra were obtained at two magnetic field positions, 3 G apart, of the Q_B^- EPR line (indicated by arrows on the inset). The difference spectrum is shown at the bottom.

different conditions. The observed differences are then interpreted as divergence in protein environment, as monitored by the proton environments near Q_B^-. For example, Mims-type ENDOR was applied to look for conformational differences near Q_B^- between two different RCs. The three-dimensional crystal structure of RCs from *B.* viridis (*43*) and *R. sphaeroides* (*1*, *3*, *51*) are known to high resolution, and the Q_B binding pockets differ in their surrounding protein environments. Thus, as a test of matrix ENDOR to differentiate protein environments, the D-band Mims-type ENDOR of Fe-removed/Zn-replaced RCs substituted with deuterated UQ-10 for RCs from *B. viridis* and *R. sphaeroides* were obtained (Figure 7A,B). The difference spectrum (Figure 7C) demonstrates that HF matrix ENDOR is sensitive to the differing details of the Q_B proton environments of the protein for the *R. sphaeroides* and *B. viridis* RCs (Figure 7D).

In *R. sphaeroides* RCs, Q_A and Q_B are both ubiquinone-10 molecules, but crystal structures show that the protein environments of the two quinones are significantly different (*1*−*3*). The two quinones differ in hydrogen-bonding contacts with the protein, and the Q_B site is more polar than the Q_A site. This difference in H-bonding is reflected in the shift of the g_x component of the Q_B *g*-tensor to higher magnetic field as compared to the g_x value of Q_A^- ((*44*), Table 1). As a result of their different binding characteristics, these quinones have different redox potentials. Q_A accepts only one electron and no protons, whereas Q_B can be doubly reduced and protonated to form the hydroquinone (*52*). The D-band Mims-type ^{1}H ENDOR spectrum of chemically reduced Q_A^- was obtained. The Q_A^- spectrum represents the dark state of the RC, and as we have shown recently, this spectrum is quite distinct from the time-resolved, light-induced, spin-correlated radical pair ENDOR spectrum of Q_A^- (however, in this latter case, Q_A^- is interacting with P^+) (*38*, *50*). The

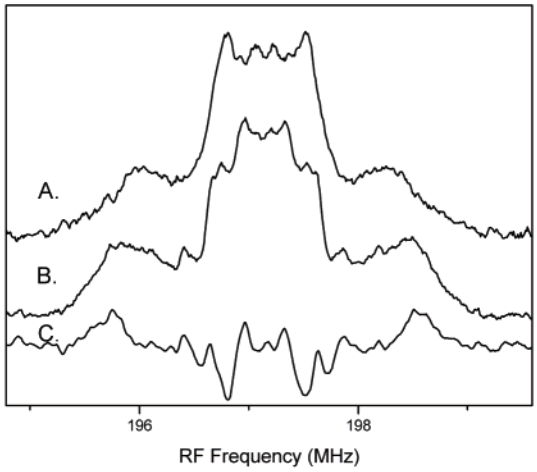

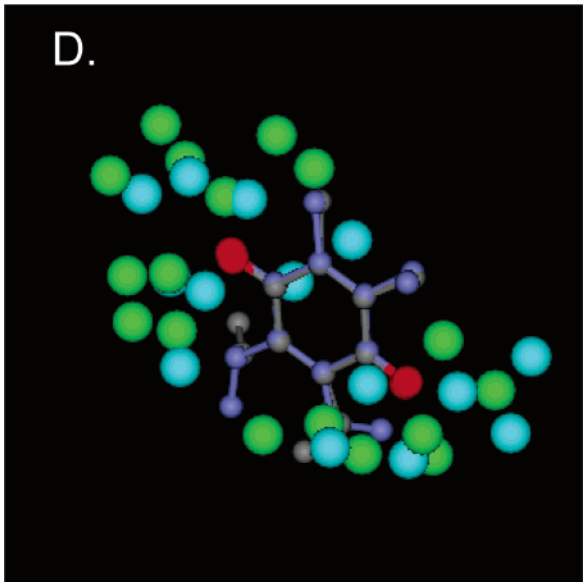

FIGURE 7: Comparison of D-band Mims-type ^{1}H ENDOR of the Q_B^- binding sites for *R. sphaeroides* and *B. viridis* RCs. The ^{1}H ENDOR spectra obtained at a magnetic field position of 46364 G for deuterated Q_B^- in RCs from (A) *B. viridis* and (B) *R. sphaeroides*. (C) A difference spectrum of A − B is shown in (C). The differences in the protein environments as observed with HF ^{1}H ENDOR spectroscopy of the proton environments for each RC from different bacterial species is reflected in the difference spectrum C. (D) Protons within a 4 Å sphere around each of the carbonyl oxygens (red) of Q_B, as determined from the X-ray crystallographic structures of the *R. sphaeroides* RC (1pcr) (*3*) and *B. viridis* RC (2prc) (*33*). The structures of Q_B from each RC were overlapped, and only protons from amino acids in the local Q_B environments of the *B. viridis* RC (aqua) and *R. sphaeroides* RC (green) are shown.

observed spectrum of chemically reduced Q_A^- is distinct from the spectrum of Q_B^- (Figure 8), displaying the sensitivity of the HF matrix ENDOR technique to different ubiquinone binding pockets.

Protein Environment Near Q_B^- in R. sphaeroides RCs: Influence of Trapping Conditions. The Q_B^- environment of samples cooled by different freezing methods was examined with HF matrix ENDOR. The similar spectra indicate that no differences in protein structure near Q_B^- in *R. sphaeroides* RCs were observed when samples were trapped under the different conditions of the laser light regime (Figure 9A) versus the red light regime (data not shown). Thus, the RCs appear to exist in the same conformational substate near Q_B^-

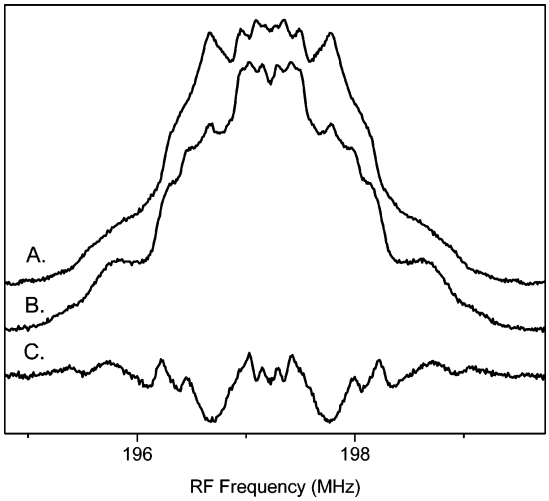

FIGURE 8: Comparison of D-band Mims-type ^{1}H ENDOR of Fe-removed/Zn-replaced RCs for different quinone binding pockets. The ^{1}H ENDOR spectra obtained at a magnetic field position of 46384 G for deuterated ubiquinone-10 in the Q_A (A) and the Q_B (B) binding sites of *R. sphaeroides* reflect the differences in the protein environments for the two distinct quinone binding sites. Spectrum C shows the difference spectrum of A − B.

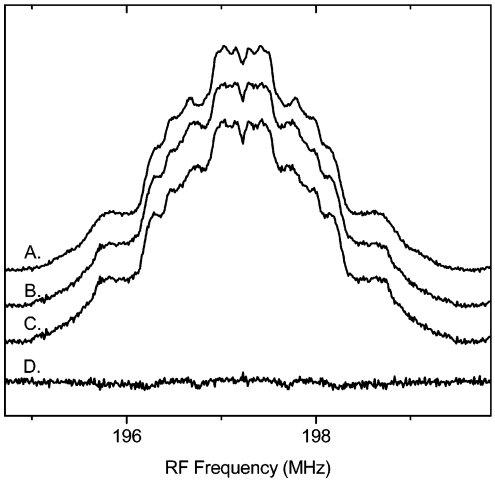

FIGURE 9: D-band Mims-type ^{1}H ENDOR of RCs from *R. sphaeroides*. No structural differences in protein structure near Q_B^- were observed for the different kinetic $P^+Q_B^-$ states of the RC. (A) ^{1}H ENDOR spectrum of "inactive" Q_B^- site observed by cooling the sample to 20 K under 1 Hz, 605 nm laser excitation. (B) ^{1}H ENDOR spectrum of the "active" Q_B^- site obtained for RCs frozen after exposure to red light at room temperature, then quenched at 170 K for 60 min. The ENDOR spectrum was collected under 10 Hz, 605 nm laser excitation at 20 K. (C) Spectrum B − 20% contribution of the ^{1}H ENDOR spectrum of Q_A^- (Figure 8A). (D) Difference spectrum of spectrum A − spectrum C showing that the differences observed in spectrum B are the result of a ∼20% contribution from Q_A^- incurred by 10 Hz laser excitation. All spectra were obtained at a magnetic field position of 46384 G.

under either freezing condition for the inactive $P^+Q_B^-$ state trapped at 20 K.

The Q_B^- environment of the active $P^+Q_B^-$ state, wherein the low-temperature interquinone electron transfer proceeds, was examined by recording the HF ENDOR spectrum under continuous 10 Hz laser flashing at 20 K for a RC sample that was frozen in the light and subsequently quenched at 170 K (Figure 9B). The HF ENDOR spectrum of the Q_B^- environment of the original active $P^+Q_B^-$ state trapped at 20 K (the sample was not warmed to higher temperatures) observed under continuous laser flashing at 20 K was essentially identical to the spectrum shown in Figure 9B (data not shown). The ^{1}H ENDOR spectra of Q_B^- obtained for the inactive $P^+Q_B^-$ conformation (Figure 9A) versus the active $P^+Q_B^-$ state (Figure 9B) produced by low-temperature annealing were different. These differences either could reflect variations in protein structure at Q_B^- for the inactive versus the active states or could simply result from the overlap of a small component of Q_A^- signals. A 20% contribution from Q_A^- was estimated from the simulation of the EPR spectrum recorded under continuous laser flashing conditions at 20 K (Figure 4). To determine the extent that this 20% Q_A^- contribution affects the difference between the spectra of the two reaction center states, we subtracted a 20% contribution of the Q_A^- ENDOR spectrum from the spectrum obtained in Figure 9B for the active $P^+Q_B^-$ (Figure 9C). As evidenced in the difference spectrum (Figure 9D) the observed difference between spectra in Figure 9A and Figure 9B results from a 20% contribution of Q_A^-. Therefore, there is no change, within the resolution of these experiments, in the spectra of Q_B^- for the inactive and active states. No significant changes in the protein environment at Q_B^- were observed between these kinetically distinct $P^+Q_B^-$ states.

DISCUSSION

In this study, we have used HF pulsed EPR and ENDOR to explore the possibility that local protein structure changes in the Q_B environment enable the $Q_A^-Q_B \rightarrow Q_AQ_B^-$ electron-transfer reaction to proceed at low temperatures. The *g*-tensor resolution of Q_A^- and Q_B^- at HF EPR allows us to spectroscopically distinguish these radical species, enabling the selective HF ENDOR of Q_B^- and Q_A^- sites to be obtained. These magnetic resonance techniques provide concomitant structural and kinetic information in noncrystalline samples, allowing the local protein environment surrounding Q_B^- to be examined in functionally defined states.

RCs Trapped in a Light-Adapted Inactive $P^+Q_B^-$ Conformation. Two distinct kinetic states of $P^+Q_B^-$ were detected with HF EPR at 20 K in both *R. sphaeroides* and *B. viridis* RCs: an active $P^+Q_B^-$ state and an inactive $P^+Q_B^-$ state. This is the first report of the low-temperature trapping of an inactive $P^+Q_B^-$ state. The population of RCs in the trapped inactive $P^+Q_B^-$ state is dependent on the light-trapping procedure used during freezing of the RC. As the temperature of the sample is warmed, the inactive $P^+Q_B^-$ fraction recombines to the ground-state PQ_B and light-induced activity is restored. Thus, the protein is not damaged by the methods for trapping $P^+Q_B^-$, but rather the inactive $P^+Q_B^-$ state is a distinct conformational state of the protein that inhibits low-temperature charge recombination. With optical experiments utilizing flash-induced optical absorbance transients to monitor the differences in P and P^+ absorbances, an inactive state where P^+ remains oxidized at low temperatures was observed (*12*, *15*, *53*). This trapped P^+ was thought to represent RCs frozen in a $P^+Q_AQ_B$ state where the concurrently generated reduced quinone has been oxidized by adventitious mediators (*15*). Our results suggest that the trapped P^+ state observed optically could in fact be the inactive $P^+Q_AQ_B^-$ state we have observed with our EPR experiments, as reduced quinone species are difficult to detect with difference optical absorption measurements. Future temperature-dependence studies will address the nature of the origin of the large differences

in recombination rates between the inactive and active $P^+Q_B^-$ states, for example, free energy, reorganization energy, or electronic coupling (*10*). Previously, biphasicities of the $P^+Q_A^-$ and $P^+Q_B^-$ charge recombination kinetics have been observed for RCs from several bacterial species, including both *B. viridis* and *R. sphaeroides* (*54*−*60*). The kinetically distinct conformational states with regards to "fast" and "slow" phases of $P^+Q_B^-$ charge recombination could be related to the inactive and active $P^+Q_B^-$ states we observe at low temperature under light-trapping conditions.

Low-Temperature $Q_A^-Q_B \rightarrow Q_AQ_B^-$ Electron Transfer in B. viridis and R. sphaeroides RCs: The Active $P^+Q_B^-$ Conformation. As shown here, the low-temperature $Q_A^-Q_B \rightarrow Q_AQ_B^-$ electron-transfer event can be monitored with HF EPR techniques due to resolved *g*-tensors of the P^+, Q_A^-, and Q_B^- signals. EPR allows us to examine the decay of the quinone anion states as well as the decay and formation of P^+, thus, providing complementary information to that obtained by transient optical measurements. Our EPR results support the earlier optical work (*12*, *15*): *R. sphaeroides* RCs with bound Q_B frozen under illumination adopt a conformation that supports electron transfer from Q_A to Q_B, and this reaction proceeds with a significant yield even at 20 K. The long recombination time of the $P^+Q_B^-$ radical pair makes the direct measurement of the rate of $Q_A^-Q_B \rightarrow Q_AQ_B^-$ electron transfer at low-temperature unrealistic for the EPR experiment. With optical experiments, the electron-transfer rate was estimated to be faster than 10^3 s^{-1} at 40 K (*12*).

The *B. viridis* RC protein appears to behave similarly to the *R. sphaeroides* RC protein in terms of low-temperature $Q_A^-Q_B \rightarrow Q_AQ_B^-$ reaction: low-temperature electron transfer does not occur for the dark-adapted conformation of the protein but does occur for a light-induced protein conformation. Thus, light-induced structural changes can be trapped cryogenically to enable low-temperature $Q_A^-Q_B \rightarrow Q_AQ_B^-$ electron transfer in *B. viridis* RCs. Because *B. viridis* and *R. sphaeorides* RCs exhibit low sequence homology, the protein conformational changes that occur upon freezing in the light are perhaps more global in nature than localized changes in specific amino acid residues. Whereas the *g*-tensors of Q_B^- (Table 1) determined with HF EPR indicate similar electronic structures for the Q_B environments in *B. viridis* and *R. sphaeorides* RCs, HF ENDOR spectra reflect differences in surrounding protein environments of the two Q_B binding pockets (Figure 7).

RCs from *B. viridis* and *R. sphaeroides* both have a non-heme Fe^{2+} situated between Q_A and Q_B. Previous reports showed that substitution of different divalent metal ions into the Fe site did not significantly alter the room-temperature $Q_A^-Q_B \rightarrow Q_AQ_B^-$ electron-transfer characteristics in *R. sphaeroides* RCs (*61*). A similar study of the influence of Fe-removal in *B. viridis* RC has not been done. Our experiments require the removal of the Fe^{2+} and replacement with diamagnetic Zn^{2+}. Thus, Fe^{2+} is not essential for $Q_A^-Q_B \rightarrow Q_AQ_B^-$ electron transfer in *R. sphaeroides* and *B. viridis* RCs, at least at low temperature, as shown by HF EPR. A recent report suggested that Q_B is not reduced directly by Q_A^- but presumably through an intermediary electron donor (*62*). On the basis of our results, Fe^{2+} does not act as an intermediate electron donor to Q_B^- at low temperature.

HF "Matrix" ENDOR as a Tool for Detecting Protein Conformational Changes. What is the nature of the light-induced conformational changes that enable low-temperature electron transfer? We have approached this question from the standpoint of the ENDOR experiment by developing methods to examine local protein environments surrounding the quinones in isotopically substituted samples as well as changes in the positions of the quinones. Substitution of deuterated quinone into protonated RCs allows us to observe ENDOR spectra solely of the protons in the matrix surrounding the quinone, ^1H nuclei from the protein environment and bound water molecules that have hyperfine interactions with the electronic spin of ^2H Q_B^-. Because of the multitude of ^1H amino acids in the protein matrix, the observed matrix ^1H ENDOR is composed of numerous overlapping resonances.

The number of contributing ^1H amino acids observed by ENDOR experiments was estimated by first determining the distance range of the local protein environment that HF Mims-type ENDOR is sensitive to. When a point-dipole approximation (*63*) is used, the anisotropic HFI constants of the ^1H are given by the following equation:

$$T = C\,\rho_0^{\pi}/R^3(3\cos^2\theta - 1)$$

where, ρ_0^{π} is the carbonyl oxygen π−spin density of the unpaired electron and $C = g_e g_N \beta_e \beta_N / h = 79.2$ MHz·Å^3. Here, g_e and g_N are the electron and nuclear *g*-values, β_e and β_N are the electron and nuclear Bohr magnetons, and θ is the angle between the applied magnetic field and the vector directed to the particular hydrogen atom. From this equation, the maximum distance *R* at which a proton still contributes to the ^1H ENDOR spectrum can be estimated. For simplicity, we replace the angle factor by 1. The minimum coupling, *T*, was estimated from the ENDOR spectra (Figure 7) to be ∼0.15−0.2 MHz. In the case of semiquinone radicals, ∼50% of the spin density is located on the two carbonyl oxygens (*45*). Assuming that spin density is localized only on the carbonyl oxygens (25% on each), we estimate that ENDOR spectra are sensitive to protons located within a sphere $R =$ 4.5−5 Å around each oxygen.

The number of protons within these spheres was estimated by analysis of the X-ray crystallographic structures of *R. sphaeroides* (*3*) and *B. viridis* (*33*) RCs. In our samples, Q_B is deuterated and does not contribute any protons. On the basis of the crystal structures, the number of the amino acid residue protons within spheres of radius $R = 4$, 5, and 6 Å around carbonyl oxygens for *R. sphaeroides* RCs are 17, 37, 61 and, for *B. viridis* RCs, 15, 39, and 60, respectively. Figure 7D depicts the proton positions within an $R = 4$ Å sphere for *R. sphaeroides* and *B. viridis* RCs by overlapping quinone structures. Even though a comparable number of protons, with a similar distribution, contribute to the ^1H ENDOR spectra of *R. sphaeroides* and *B. viridis* RCs, distinct differences in the spectral ENDOR line shapes are observed (Figure 7C). These spectral differences illustrate the high sensitivity of HF Mims-type ENDOR to local protein environments. Therefore, any local differences between the Q_B^- environments for the inactive and active $P^+Q_B^-$ states, as reflected in different proton locations near Q_B^-, should be detectable with HF ENDOR.

Note, Mims-type ENDOR spectra differ from typical Davis-type spectra that contain a discernible number of resonances resulting from stronger hyperfine interactions, such as H-bonds to Q_B^-. Although the disadvantage of Mims-type ENDOR is that direct assignment of resonances is nearly impossible without site-directed mutagenesis or more selective isotopic substitutions, the prevailing advantage is that a broad region of the protein environment (~4.5−5 Å from the quinone carbonyl oxygens) can be examined for changes that result from a number of factors, such as freezing conditions, pH, metal ion binding, or solvent viscosity. Experimental results reported here show that different proton environments are detectable with the HF matrix ENDOR technique. Distinct ENDOR spectra were observed for the Q_B^- environments of RCs from *R. sphaeroides* and *B. viridis* as well as for the Q_A^- versus Q_B^- sites of *R. sphaeroides* RCs. Furthermore, the orientational selectivity of the HF ENDOR shows that this experiment is sensitive to reorientation of the quinone (within 5°).

Investigating the Q_B^- Site of Functionally Defined States of $P^+Q_B^-$ with HF EPR/ENDOR. Unlike crystallography, EPR provides concomitant structural and kinetic information on proteins in solution. Analysis of the light-induced radical species allows association of conformational states with function. Thus, we have examined the ENDOR of Q_B^- in the active and inactive $P^+Q_B^-$ states to see if the conformational change that controls reactivity resides in the Q_B local environment.

No changes in the proton environment near Q_B^- were observed with matrix ENDOR for RCs in the inactive $P^+Q_B^-$ state compared to the active $P^+Q_B^-$ state. On the basis of our data, we can rule out any significant displacement or reorientation (within 5°) of Q_B^- in the active versus the inactive sites. Surprisingly, the proton environment surrounding Q_B^-, as examined by HF Mims-ENDOR, did not change for different preparations of Fe-removal/Zn-replacement, for different pHs (pH 10, 8, and 5.5 at room temperature), or for samples in H_2O-based versus D_2O-based buffer systems. Furthermore, no differences in the Davies ^{1}H ENDOR of Q_B^- were observed for the inactive versus active states (data not shown). Thus, the protein environment, as observed by the ^{1}H matrix surrounding the semiquinone Q_B^-, is quite stable and resistant to conformational changes in response to different conditions. Modifying the isotopic composition of the sample, for example, ^{1}H ENDOR of fully deuterated RCs in H_2O (*38*), will help simplfy the ENDOR spectrum, and more specific responses of the protein environment to different protonation states of residues near Q_B, such as Glu-212, may be detectable.

Are any conformational intermediates of Q_B^- observed when the sample temperature is warmed above 20 K? RCs frozen in the light were warmed to different temperatures to examine potential conformational states intermediate between the neutral dark state Q_B and the light-trapped active state of Q_B^-. Different conformational states along the reaction path have been reported previously (*12*). In these optical experiments, when the temperature of light-adapted RCs is raised above 120 K, the trapped conformation which can form $P^+Q_B^-$ relaxes to an inactive conformation which is different from the RCs frozen in the dark (*12*). Herein, EPR spectra reveal a time-dependent decrease in the trapped inactive Q_B^- signal upon warming the RCs to 170 K or above. When cooled back down to 20 K, approximately 50% of the RCs were in an active intermediate state, transferring electrons between Q_A^- and Q_B. The recombination kinetics of this active intermediate state are different than the kinetics of the active state trapped initially at 20 K. This observed difference in recombination kinetics suggests that the active intermediate $P^+Q_B^-$ state is truly in a different conformational substate than the active $P^+Q_B^-$ state. However, HF ENDOR spectra indicate that any structural differences between these two conformational substates are not situated in the local protein environment surrounding Q_B^-.

These results are consistent with tight binding of Q_B in the semiquinone state (*64*). A strong binding affinity of the semiquinone Q_B^- might explain the well-defined position of Q_B in crystals of RCs cryotrapped in the light-adapted state (*18*, *34*, *65*). This is a much different situation than dark neutral Q_B, which has been found to be located in different positions in the various reported crystal structures (*3*, *18*, *19*, *21*, *22*, *30*, *33*, *34*). We are unable to directly examine proximal versus distal movement of Q_B in solution with EPR spectroscopy because Q_B cannot be chemically reduced without simultaneously chemically reducing Q_A. Therefore, Q_B^- in the "dark" state of the RC cannot be examined without also observing the biradical $Q_A^-Q_B^-$ (*66*). However, we can rule out any local rearrangements, such as a proximal versus distal shift of Q_B^-, for the inactive and active $P^+Q_B^-$ states because the HF ^{1}H ENDOR spectrum is sensitive to a change in H-bonding and ^{1}H hyperfine interactions that would accompany a 5 Å shift and 180° rotation in Q_B^- position.

Another possibility is that light-induced changes trapped at low temperature are not near Q_B at all, but rather located in the protein environment near Q_A. Solvent reorganization, conformational changes, or proton rearrangements have been postulated to stabilize the $P^+Q_A^-$ state (*67*−*70*). A semistable, charge-separated $P^+Q_A^-$ state has been observed at room temperature for RCs illuminated with bright light (*71*, *72*), and structural changes in the H protein subunit have been observed in response to bright light (*73*). Recently, we reported the observation of reorganization of the protein environment to accommodate the donor−acceptor charge separated state $P^+Q_A^-$ (*38*). Future HF ENDOR experiments will be directed at examining light-induced changes near Q_A^-. Preliminary EPR results show that we can trap both inactive and active $P^+Q_A^-$ states when RCs with Q_B inhibitors are frozen under light conditions (*74*).

In summary, we have observed two light-induced protein conformational states of $P^+Q_B^-$ at low temperature and have taken a novel approach to examine the local protein environments surrounding Q_B^- for each of these states. Two important factors for the success of these experiments are (i) samples with selective deuteration and protonation for signal resolution and selectivity and (ii) advanced HF (D-band) pulsed EPR and ENDOR instrumentation with light-induced time-resolved capabilities. Similar to *R. sphaeroides* RCs, light-induced changes in the *B. viridis* RC enable low-temperature $Q_A^-Q_B \rightarrow Q_AQ_B^-$ electron transfer. As shown here, HF matrix ENDOR is sensitive to different proton environments surrounding the quinone and to different orientations of the quinone. No structural changes near Q_B^- were observed for *R. sphaeroides* RCs frozen in inactive and active $P^+Q_B^-$ states with regards to electron transfer.

Interactions of the semiquinone Q_B^- with the protein are rigid, suggesting quite an enforced protein environment surrounding Q_B^- and that the conformational change that controls reactivity resides beyond the Q_B local environment.

REFERENCES

1. Allen, J. P., Feher, G., Yeates, T. O., Komiya, H., and Rees, D. C. (1988) Structure of the reaction center from *Rhodobactor Sphaeroides* R-26: protein cofactor (quinones and Fe^{2+}) interactions, *Proc. Natl. Acad. Sci. U.S.A. 85*, 8487−8491.
2. Chang, C. H., El-Kabbni, O., Tiede, D. M., Norris, J., and Schiffer, M. (1991) Structure of the membrane-bound protein photosynthetic reaction center from *Rhodobacter sphaeroides* R-26., *Biochemistry 30*, 5353−5360.
3. Ermler, U., Fritzsch, G., Buchanan, S., and Michel, H. (1994) Structure of the photosynthetic reaction-center from *Rhodobacter sphaeroides* at 2.65 Angstrom resolution−cofactors and protein−cofactor interactions, *Structure 2*, 925−936.
4. Parson, W. W. (1987) The bacterial reaction center, in *Photosynthesis* (Amesz, J., Ed.) pp 43−61, Elsevier, New York.
5. Feher, G., Allen, J. P., Okamura, M. Y., and Rees, D. C. (1989) Structure and function of bacterial photosynthetic reaction centers, *Nature 339*, 111−116.
6. Okamura, M. Y., Paddock, M. L., Graige, M. S., and Feher, G. (2000) Proton and electron transfer in bacterial reaction centers, *Biochim. Biophys. Acta 1458*, 148−163.
7. Mancino, L., Dean, D., and Blankenship, R. (1984) Kinetics and thermodynamics of the $P870^+Q_A^-$−$P870^+Q_B^-$ reaction in isolated reaction centers from the photosynthetic bacterium *Rhodopseudomonas sphaeroides*, *Biochim. Biophys. Acta 764*, 46−54.
8. Tiede, D. M., Vazquez, J., Cordova, J., and Marone, P. A. (1996) Time-resolved electrochromism associated with the formation of quinone anions in the *Rhodobacter sphaeroides* R26 reaction center, *Biochemistry 35*, 10763−10775.
9. Li, J., Gilroy, D., Tiede, D. M., and Gunner, M. R. (1998) Kinetic phases in the electron transfer from $P^+Q_A^-Q_B$ to $P^+Q_AQ_B^-$ and the associated processes in *Rhodobacter Sphaeroides* R-26 reaction centers, *Biochemistry 37*, 2818−2829.
10. Schmid, R., and Labahn, A. (2000) Temperature and free energy dependence of the direct charge recombination rate from the secondary quinone in bacterial reaction centers from *Rhodobacter sphaeroides*, *J. Phys. Chem. B 104*, 2928−2936.
11. Balabin, I. A., and Onuchic, J. N. (2000) Dynamically controlled protein tunneling paths in photosynthetic reaction centers, *Science 290*, 114−117.
12. Xu, Q., and Gunner, M. R. (2001) Trapping conformational intermediate states in the reaction center protein from photosynthetic bacteria, *Biochemistry 40*, 3232−3241.
13. Xu, Q., Baciou, L., Sebban, P., and Gunner, M. R. (2002) Exploring the energy landscape for Q_A^- to Q_B electron transfer in bacterial photosynthetic reaction centers: effect of substrate position and tail length on the conformational gating step, *Biochemistry 41*, 10021−10025.
14. Graige, M. S., Feher, G., and Okamura, M. Y. (1998) Conformational gating of the electron-transfer reaction $Q_A^-Q_B$−$Q_AQ_B^-$ in bacterial reaction centers of *Rhodobacter sphaeroides* determined by a driving force assay, *Proc. Natl. Acad. Sci. U.S.A. 95*, 11679−11684.
15. Kleinfeld, D., Okamura, M. Y., and Feher, G. (1984) Electron-transfer kinetics in photosynthetic reaction centers cooled to cryogenic temperatures in the charge-separated state: evidence for light-induced structural changes, *Biochemistry 23*, 5780−5786.
16. van den Brink, J. S., Hulsebosch, R. J., Gast, P., Hore, P. J., and Hoff, A. J. (1994) Q_A binding in reaction centers of the photosynthetic purple bacterium *Rhodobacter sphaeroides* R26 investigated with electron spin polarisation spectroscopy, *Biochemistry 33*, 13668−13677.
17. Bittl, R., Zech, S. G., and Lubitz, W. (1995) Light-induced changes in transient EPR spectra of $P^+Q_A^-$, in *The Reaction Center of Photosynthetic Bacteria: Structure and Dynamics* (Michel-Beyerle, M.-E., Ed.) pp 333−339, Springer-Verlag, Berlin, Germany.
18. Stowell, M. H. B., McPhillips, T. M., Rees, D. C., Soltis, S. M., Abresch, E., and Feher, G. (1997) Light induced structural changes in photosynthetic reaction center: implications for mechanism of electron−proton transfer, *Science 276*, 812−816.
19. Kuglstatter, A., Ermler, U., Michel, H., Baciou, L., and Fritzsch, G. (2001) X-ray structure analyses of photosynthetic reaction center variants from *Rhodobacter sphaeroides*: structural changes induced by point mutations at position L209 modulate electron and proton transfer, *Biochemistry 40*, 4253−4260.
20. Pokkuluri, P. R., Laible, P. D., Deng, Y.-L., Wong, T. N., Hanson, D. K., and Schiffer, M. (2002) The structure of a mutant photosynthetic reaction center shows unexpected changes in main chain orientations and quinone position, *Biochemistry 41*, 5998−6007.
21. Pokkuluri, P. R., Laible, P. D., Crawford, A. E., Mayfield, J. F., Yousef, M. A., Ginell, S. L., Hanson, D. K., and Schiffer, M. (2004) Temperature and cryoprotectant influence secondary quinone binding position in bacterial reaction centers, *FEBS Lett. 570*, 171−174.
22. Baxter, R. H. G., Ponomarenko, N., Srajer, V., Pahl, R., Moffat, K., and Norris, J. R. (2004) Time-resolved crystallographic studies of light-induced structural changes in the photosynthetic reaction center, *Proc. Natl. Acad. Sci. U.S.A. 101*, 5982−5987.
23. Breton, J., Buollais, C., Mioskowski, C., Sebban, P., Baciou, L., and Nabedryk, E. (2002) Vibrational spectroscopy favors a unique Q_B binding site at the proximal position in wild-type reaction centers and in the Pro-L209 → Tyr mutant from *Rhodobacter sphaeroides*, *Biochemistry 41*, 12921−12927.
24. Nabedryk, E., Breton, J., Sebban, P., and Baciou, L. (2003) Quinone (Q_B) binding site and protein structural changes in photosynthetic reaction center mutants at Pro-L209 revealed by vibrational spectroscopy, *Biochemistry 42*, 5819−5827.
25. Breton, J. (2004) Absence of large-scale displacement of quinone Q_B in bacterial photosynthetic reaction centers, *Biochemistry 43*, 3318−3326.
26. Vermeglio, A., and Clayton, R. K. (1977) Kinetics of electron transfer between the primary and secondary electron acceptor in reaction centers from *Rhodopseudomonas sphaeroides*, *Biochim. Biophys. Acta 461*, 159−165.
27. Takahasi, E., Maroti, P., and Wraight, C. A. (1992) Coupled proton and electron-transfer pathways in the acceptor quinone complex of reaction centers from *Rhodobacter sphaeroides*, in *Electron and Proton Transfer in Chemistry and Biology* (Muller, A., Ed.), Elsevier, New York.
28. Tiede, D. M., Utschig, L., Hanson, D. K., and Gallo, D. M. (1998) Resolution of electron and proton-transfer events in the electrochromism associated with quinone reduction in bacterial reaction centers, *Photosynth. Res. 55*, 267−273.
29. Lubitz, W., and Feher, G. (1999) The primary and secondary acceptors in bacterial photosynthesis. Characterization of the quinone radicals Q_A^- and Q_B^- by EPR and ENDOR, *Appl. Magn. Reson. 17*, 1−48.
30. Lancaster, C. R. (1999) Quinone-binding sites in membrane proteins: what can we learn from the *Rhodopseudomonas viridis* reaction centre?, *Biochem. Soc. Trans. 27*, 591−596.
31. Ravelli, R. B. G., and McSweeney, S. M. (2000) The "fingerprint" that X-rays can leave on structures, *Structure 8*, 315−328.
32. Baxter, R. H. G., Seagle, B.-L., Ponomarenko, N., and Norris, J. (2004) Specific radiation damage illustrates light-induced structural changes in the photosynthetic reaction center, *J. Am. Chem. Soc. 126*, 16728−16729.
33. Lancaster, C. R. D., and Michel, H. (1997) The coupling of light-induced electron transfer and proton uptake as derived from crystal structures of reaction centres from *Rhodopseudomonas viridis* modified at the binding site of the secondary quinone, Q_B, *Structure 5*, 1339−1359.
34. Fritzsch, G., Koepke, J., Diem, R., Kuglstatter, A., and Baciou, L. (2002) Charge separation induces conformational changes in the photosynthetic reaction centre of purple bacteria, *Acta Crystallogr. D58*, 1660−1663.
35. Feher, G. (1971) Some chemical and physical properties of a bacterial reaction center particle and its primary photochemical reactants, *Photochem. Photobiol. 14*, 373−387.
36. Loach, P. A., and Hall, R. L. (1972) The question of the primary electron acceptor in bacterial photosynthesis, *Proc. Natl. Acad. Sci. U.S.A. 69*, 786−790.
37. Utschig, L. M., Greenfield, S. R., Tang, J., Laible, P. D., and Thurnauer, M. C. (1997) Influence of iron-removal procedures on sequential electron transfer in photosynthetic bacterial reaction centers studied by transient EPR spectroscopy, *Biochemistry 36*, 8548−8558.
38. Poluektov, O. G., Utschig, L. M., Dubinskij, A. A., and Thurnauer, M. C. (2005) Electron-transfer pathways and protein response to

charge separation in photosynthetic reaction centers: time-resolved high-field ENDOR of the spin-correlated radical pair $P_{865}{}^{+}Q_A{}^{-}$, *J. Am. Chem. Soc. 127*, 4049−4059.
39. Lakshmi, K. V., Reifler, M. J., Brudvig, G. W., Poluektov, O. G., Wagner, A. M., and Thurnauer, M. C. (2000) High-field EPR study of carotenoid and chlorophyll cation radicals in Photosystem II, *J. Phys. Chem. B 104*, 10445−10448.
40. Mims, W. B. (1965) Pulsed electron nuclear double resonance (ENDOR) experiments, *Proc. R. Soc. London 283*, 452−457.
41. Davies, E. R. (1974) A new pulse ENDOR technique, *Phys. Lett. A 47*, 1−2.
42. Poluektov, O. G., Utschig, L. M., Schlesselman, S. L., Lakshmi, K. V., Brudvig, G. W., Kothe, G., and Thurnauer, M. C. (2002) Electronic structure of the P_{700} special pair from high-frequency electron paramagnetic resonance spectroscopy, *J. Phys. Chem. B 106*, 8911−8916.
43. Deisenhofer, J., Epp, O., Sinning, I., and Michel, H. (1995) Crystallographic refinement at 2.3 angstrom resolution and refined model of the photosynthetic reaction center from *Rhodopseudomonas viridis*, *J. Mol. Biol. 246*, 429−457.
44. Gardiner, A. T., Zech, S. G., MacMillan, F., Kass, H., Bittl, R., Schlodder, E., Lendzian, F., and Lubitz, W. (1999) Electron paramagnetic resonance studies of zinc-substituted reaction centers from *Rhodopseudomonas viridis*, *Biochemistry 38*, 11773−11787.
45. Sinnecker, S., Reijerse, E., Neese, F., and Lubitz, W. (2004) Hydrogen bond geometries from electron paramagnetic resonance and electron−nuclear double resonance parameters: density functional study of quinone radical anion−solvent interactions, *J. Am. Chem. Soc. 126*, 3280−3290.
46. Tang, J., Utschig, L. M., Poluektov, O., and Thurnauer, M. C. (1999) Transient W-band EPR study of sequential electron transfer in photosynthetic bacterial reaction centers, *J. Phys. Chem. 103*, 5145−5150.
47. Poluektov, O. G., Utschig, L. M., Tang, J., Dubinski, A. A., Schlesselman, S. L., and Thurnauer, M. C. (2001) High-frequency EPR approach to the electron spin-polarization effects observed in the photosynthetic reaction centers, *Appl. Magn. Reson. 21*, 311−323.
48. Thurnauer, M. C., Poluektov, O., and Kothe, G. (2004) Time-resolved high-frequency and multifrequency EPR studies of spin-correlated radical pairs in photosynthetic reaction center proteins, in *Biological Magnetic Resonance: Very High Frequency (VHF) ESR/EPR* (Grinberg, O. Y., and Berliner, L. J., Eds.) pp 165−206, Kluwer Academics, New York.
49. Goldfarb, D., and Arieli, D. (2004) Spin distribution and the location of protons in paramagnetic proteins, *Annu. Rev. Biophys. Biomol. Struct. 33*, 441−468.
50. Poluektov, O. G., Utschig, L. M., Dubinskij, A. A., and Thurnauer, M. C. (2004) ENDOR of spin-correlated radical pairs in photosynthesis at high magnetic field: a tool for mapping electron-transfer pathways, *J. Am. Chem. Soc. 126*, 1644−1645.
51. El-Kabbani, O., Chang, C.-H., Tiede, D. M., Norris, J., and Schiffer, M. (1991) Comparison of reaction centers from *Rhodobacter sphaeroides* and *Rhodopseudomonas viridis*: overall architecture and protein−pigment interactions, *Biochemistry 30*, 5361−5369.
52. Wraight, C. A. (2004) Proton and electron transfer in the acceptor quinone complex of photosynthetic reaction centers from *Rhodobacter sphaeroides*, *Front. Biosci. 9*, 309−337.
53. McElroy, J. D., Mauzerall, D. C., and Feher, G. (1974) Characterization of primary reactants in bacterial photosynthesis. II. Kinetic studies of the light-induced EPR signal ($g = 2.0026$) and the optical absorbance changes at cryogenic temperatures, *Biochim. Biophys. Acta 333*, 261−277.
54. Parot, P., Thiery, J., and Vermeglio, A. (1987) Charge recombination at low temperature in photosynthetic bacterial reaction centers: evidence for two conformational states, *Biochim. Biophys. Acta 893*, 534−543.
55. Sebban, P. (1988) pH effect on the biphasicity of $P^{+}Q_A{}^{-}$ charge recombination kinetics in reaction centers from *Rhodobacter sphaeroides* reconstituted with anthraquinone, *Biochim. Biophys. Acta 936*, 124−132.
56. Sebban, P., and Wraight, C. A. (1989) Heterogeneity of the $P^{+}Q_A{}^{-}$ recombination kinetics in reaction centers from *Rhodopseudomonas viridis*: effect of pH and temperature, *Biochim. Biophys. Acta 974*, 54−65.
57. Baciou, L., Rivas, E., and Sebban, P. (1990) $P^{+}Q_A{}^{-}$ and $P^{+}Q_B{}^{-}$ charge recombinations in *Rhodopseudomonas viridis* chromatophores and in RCs reconstituted in phosphatidylcholine liposomes. Existence of two conformational states of the RCs and effects of pH and *o*-phenanthroline, *Biochemistry 29*, 2966−2976.
58. Gao, J. L., Shopes, R. J., and Wraight, C. A. (1991) Heterogeneity of kinetics and electron-transfer equilibria in the bacteriopheophytin and quinone electron acceptors of reaction centers from *Rhodopseudomonas viridis*, *Biochim. Biophys. Acta 1056*, 259−272.
59. Sebban, P., Parot, P., Baciou, L., Mathis, P., and Vermeglio, A. (1991) Effects of low temperature and lipid rigidity on the charge recombination process in *Rps. viridis* and *Rb. sphaeroides* reaction centers, *Biochim. Biophys. Acta 1057*, 109−114.
60. Baciou, L., and Sebban, P. (1995) Heterogeneity of the quinone electron acceptor system in bacterial reaction centers, *Photochem. Photobiol. 62*, 271−278.
61. Debus, R. J., Feher, G., and Okamura, M. Y. (1986) Iron-depleted reaction centers from *Rhodopseudomonas sphaeroides* R-26: characterization and reconstitution with Fe^{2+}, Mn^{2+}, Co^{2+}, Ni^{2+}, Cu^{2+}, and Zn^{2+}, *Biochemistry 25*, 2276−2287.
62. Remy, A., and Gerwert, K. (2003) Coupling of light-induced electron transfer to proton uptake in photosynthesis, *Nat. Struct. Biol. 10*, 637−644.
63. Schweiger, A., and Jeschke, G. (2001) *Principles of Pulsed Electron Paramagnetic Resonance*, Oxford University Press, Oxford, U.K.
64. McPherson, P. H., Okamura, M. Y., and Feher, G. (1990) Electron transfer from the reaction center of *Rb. sphaeroides* to the quinone pool: doubly reduced Q_B leaves the reaction center, *Biochim. Biophys. Acta 1016*, 289−292.
65. Axelrod, H. L., Abresch, E. C., Paddock, M. L., Okamura, M. Y., and Feher, G. (2000) Determination of the binding sites of the proton-transfer inhibitors Cd^{2+} and Zn^{2+} in bacterial reaction centers, *Proc. Natl. Acad. Sci. U.S.A. 97*, 1542−1547.
66. Calvo, R., Abresch, E. C., Bittl, R., Feher, G., Hofbauer, W., Isaacson, R. A., Lubitz, W., Okamura, M. Y., and Paddock, M. (2000) EPR study of the molecular and electronic structure of the semiquinone biradical $Q_A{}^{-}Q_B{}^{-}$ in photosynthetic reaction centers from *Rhodobacter sphaeroides*, *J. Am. Chem. Soc. 122*, 7327−7341.
67. McPherson, P. H., Nagarajan, V., Parson, W. W., Okamura, M. Y., and Feher, G. (1990) pH-dependence of the free-energy gap between DQ_A and $D^{+}Q^{-}{}_A$ determined from delayed fluorescence in reaction centers from *Rhodobacter spheroides* R-26, *Biochim. Biophys. Acta 1019*, 91−94.
68. Franzen, S., and Boxer, S. G. (1993) Temperature-dependence of the electric field modulation of electron-transfer rates—charge recombination in photosynthetic reaction centers, *J. Phys. Chem. 97*, 6304−6318.
69. Breton, J., and Nabedryk, E. (1998) Proton uptake upon quinone reduction in bacterial reaction centers: IR signature and possible participation of a highly polarizable hydrogen bond network, *Photosynth. Res. 55*, 301−307.
70. Di Donato, M., Peluso, A., and Villani, G. (2004) Electron transfer between quinones in photosynthetic reaction centers, *J. Phys. Chem. B 108*, 3068−3077.
71. van Mourik, F., Reus, M., and Holzwarth, A. R. (2001) Long-lived charge-separated states in bacterial reaction centers isolated from *Rhodobactoer sphaeroides*, *Biochim. Biophys. Acta 1504*, 311−318.
72. Andreasson, U. and Andreasson, L.-E. (2003) Characterization of a semi-stable, charge-separated state in reaction centers from *Rhodobacter sphaeroides*, *Photosynth. Res. 75*, 223−233.
73. Katona, G., Snijder, A., Gourdon, P., Andreasson, U., Hansson, O., Andreasson, L.-E., and Neutze, R. (2005) Conformational regulation of charge recombination reactions in a photosynthetic bacterial reaction center, *Nat. Struct. Mol. Biol. 12*, 630−631.
74. Utschig, L. M. and Poluektov, O. G. (2005) unpublished results.

BI051060Q